Butterfly-shape hourglass type-II nodal birdcage and multiple quadratic nodal-line phonons in BaXN$_2$ (X = Ti, Zr, Hf)

Xiang-Feng Yang,[1] Zhe-Qi Wang,[1] and Hua-Hua Fu[1,2,*]

[1]*School of Physics and Wuhan National High Magnetic Field Center, Huazhong University of Science and Technology, Wuhan 430074, China*
[2]*Institute for Quantum Science and Engineering, Huazhong University of Science and Technology, Wuhan, Hubei 430074, China*

(Received 30 November 2023; accepted 12 January 2024; published 11 April 2024)

The exploration of various topological nodal-line phonons with novel topological properties and unique geometrical configurations has long been considered one of the central topics in topological physics. In this work we find that Weyl nodal lines are composed of two basic categories, i.e., linear and quadratic. According to the dispersion relations of degeneracy points in them, both linear and quadratic nodal lines can be divided into three types, i.e., types I, II, and III. Based on these basic types, two unusual nodal lines, i.e., anisotropic and hybrid, may be defined here. Unfortunately, real materials which may simultaneously generate these basic and unusual nodal-line phonons with different types and categories have still rarely been reported, owing to the highly required symmetry conditions. By using symmetry analysis and first-principles calculations, we uncover that a material family BaXN$_2$ (X= Ti, Zr, Hf) in space group 129 may generate novel butterfly-shape nodal-birdcage phonons that are composed of three hourglasslike type-II nodal rings and four straight nodal lines. More importantly, multiple unusual nodal lines, including anisotropic and hybrid ones, also exist in these materials. The topologically nontrivial features of these various nodal-line phonons are confirmed by the nonzero Berry phases and the drumheadlike surface states. Our theoretical results provide an ideal material platform to study the topological properties of various nodal-line phonons, including three unusual types.

DOI: 10.1103/PhysRevB.109.155414

I. INTRODUCTION

Thanks to the intense studies on topological quasiparticles both in electronic and bosonic systems [1–11], a series of topologically excited states, including Weyl nodal points [12–19], nodal lines [20–24], and nodal walls [25–29], etc., have been predicted in theory, and some of them have been confirmed in experiments [10–16]. To develop further this research topic, the exploration of unusual topological quasiparticles with unique nontrivial features towards specific device applications has already been one of the central topics in topological physics. Among them, nodal lines play a particular role in topological states and thus have long attracted researchers' particular attention [30–38]. An important reason is that nodal lines can be considered as the fundamental units to construct higher-dimensional topological states such as nodal surfaces and walls, and upon breaking special symmetries, they are opened easily to form Weyl points, Dirac points, and other topological quasiparticles [39], accompanied with interesting topological phase transitions.

We well know that nodal lines are relatively rich and complex, because they may display various geometric configurations, including nodal chain, ring, net, cage, straight lines, and others [40–42], making the researchers in this topic work as magical painters wandering in the world of topological states. Moreover, nodal lines having different geometries open up a door for understanding the fundamental physics of various topological excitations, helping us to design and fabricate various topological materials to realize topological device applications. However, the understanding into fundamental physics of node lines is still far inferior to that of node points. Taking Weyl nodal points as examples, based on their dispersion relations, we have already divided them into three basic types, i.e., types I, II, and III. Unfortunately, the similar basic categories on nodal lines have rarely been put forward. In this work we find that according to the low-energy dispersion relations in nodal lines, they can be divided into three categories, i.e., linear, quadratic, and cubic ones. Note that the cubic nodal lines are difficult to exist in real materials due to their limited symmetries; we thus recognize that nodal lines have two basic categories. Considering further the spatial distributions of these low-energy bands, both linear and quadratic nodal lines can be divided into three basic types, referred to as types I, II, and III, as illustrated in Fig. 1. Furthermore, based on these three basic types, we may further explore some unusual nodal lines. For instance, as for a nodal line, along different momentum directions of the same degeneracy points, the low-energy dispersion displays completely different types. Obviously, this nodal line cannot be simply classified into any one type listed above, so we then refer to it as an "anisotropic" nodal line. On the other hand, when the dispersion relation of one section of nodal line displays one type while in other sections of the same nodal line it behaves as a completely different type, we refer to this nodal line as a "hybrid" one [43]. These basic and further classifications are helpful for us to explore some unusual topological nodal lines in nature, and this classification ideology can be extended to other

*hhfu@hust.edu.cn

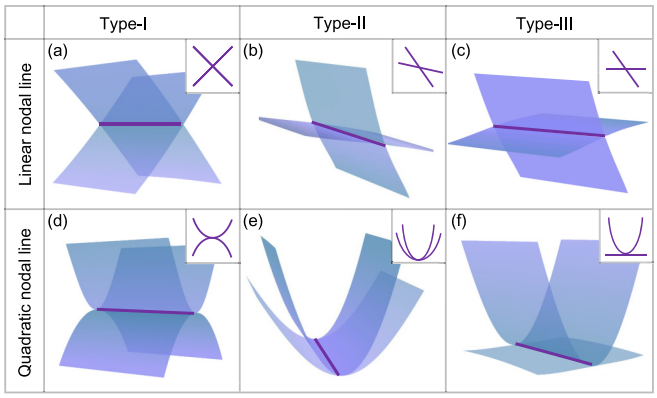

FIG. 1. The top panel, including figures (a) and (b), shows three types of liner nodal lines. The bottom panel, including figures (d) and (f), shows three types of quadratic nodal lines. Here the definition of types I, II, and III is according to the low-energy dispersion relations of degeneracy points in nodal lines as illustrated in the upper-right corner of each figure.

classes of nodal lines, including nodal ring, chain, cage, and net, etc.

In order to demonstrate the existence of various basic types of linear and quadratic nodal lines and to further explore unusual nodal lines, including anisotropic and hybrid ones rarely reported in real materials, in this work, by using symmetry analysis, low-energy effective $k \cdot p$ model, and first-principles calculations, we uncover that a material family BaXN$_2$ (X=Ti, Zr, Hf) [44,45] in space group (SG) 129 can generate a rare butterfly-shape nodal birdcage composed of three hourglasslike type-II nodal rings and four straightly linear nodal lines in their phononic spectra. It should be stressed that the nodal-birdcage phonons uncovered here are composed by different kinds of nodal-line phonons and are much different from some nodal-cage and nodal-frame phonons reported previously in Refs. [46,47], which are mainly composed by two two-dimensional (2D) nodal surfaces connected with four or six nodal lines. Thus the nodal birdcage in the present work has an advantage for studying the basic classifications and the related Berry phase of all the nodal lines to construct the nodal birdcage. More interestingly, owing to the protections from the screw rotation symmetry ($\widetilde{C}_{4z}$) and the mirror symmetry ($\mathcal{M}_x$), two unusual nodal lines, i.e., the anisotropic and hybrid quadratic nodal lines, also exist in these materials. Additionally, two pairs of unusual linear nodal lines, which display opposite Berry phases and are localized in the k_z=0 plane, are adjacent to the boundaries of Brillouin zone (BZ).

The remainder of this paper is organized as follows. In Sec. II, by using symmetry analysis we present the required symmetry conditions and the related effective low-energy $k \cdot p$ Hamiltonian models for various linear and quadratic nodal lines. In Sec. III, through systematically analyzing the phonon spectra of some real materials BaXN$_2$ (X = Ti, Zr, Hf) in SG 129 [44,45], we find that a novel butterfly-shape nodal birdcage together with three unusual nodal lines appear in these family materials, and their topologically nontrivial features are confirmed by their Berry phases and the related drumhead-like surface states in surface BZs. Finally, some concluding remarks are summarized in Sec. IV.

II. SYMMETRY ANALYSIS, CRYSTAL STRUCTURES, AND CALCULATION METHODS

First of all, we should establish low-energy $k \cdot p$ Hamiltonian models to describe the topologically nontrivial features of quadratic nodal lines, since the low-energy model for linear nodal lines is relatively easy to understand. By using symmetry analysis, we find that various types of quadratic nodal lines can be described effectively by a two-band model. To enhance the applicability of this model, we will consider fully the anisotropic and other characteristics appearing in the nodal lines. Moreover, we focus our discussion on the high-symmetry path (Γ-Z) in the three-dimensional (3D) BZ of SG 129, which are constrained both by the screw rotation symmetry ($\widetilde{C}_{4z}$) and the mirror symmetry ($\mathcal{M}_x$), to establish the effective models.

As the two band branches which are attributable to form the degeneracy points of quadratic nodal lines are very close with each other around a frequency value with k_{wp}, the following 2 × 2 Hamiltonian model can be used to describe these degeneracy points:

$$\mathcal{H}_{kp} = f_0(q)\sigma_0 + f_x(q)\sigma_x + f_y(q)\sigma_y + f_z(q)\sigma_z, \tag{1}$$

where $q = k - k_{wp}$ denotes the wave vector relative to the typical frequency value k_{wp}. Moreover, under the mirror symmetry $\mathcal{M}_x$ and considering the constraint from the screw rotation symmetry $\widetilde{C}_{4z}$, the above effective Hamiltonian should obey the following relation:

$$\widetilde{C}_{4z}\mathcal{H}_{kp}(q)\widetilde{C}_{4z}^{-1} = \mathcal{H}(-q_y, q_x, q_z). \tag{2}$$

Taking the eigenvalues of the operator matrix $\widetilde{C}_{4z}$ for those two bands along the high-symmetry line Γ-Z and under the 2D irreps R5, the matrix $\widetilde{C}_{4z}$ can be written as

$$\widetilde{C}_{4z} = \begin{bmatrix} e^{i\pi/2} & 0 \\ 0 & e^{-i\pi/2} \end{bmatrix}.$$

Then the symmetry operator $\mathcal{M}_x$ is applied to further constrain the Hamiltonian as below:

$$M_x\mathcal{H}_{kp}(q)M_x^{-1} = \mathcal{H}(-q_x, q_y, q_z). \tag{3}$$

Furthermore, we adopt the similar operation on the Hamiltonian by further considering the mirror symmetry $\mathcal{M}_x$ along this high-symmetry path Γ-Z. Note that the matrix $\mathcal{M}_x$ is described as

$$\mathcal{M}_x = \begin{bmatrix} 1 & 0 \\ 0 & -1 \end{bmatrix}.$$

Finally, the symmetry-permitted expression for quadratic nodal lines as a function of q to the lowest orders can be written as

$$\begin{aligned}\mathcal{H}_{kp} = {} & a_{12}q_xq_y\sigma_x + b_{12}q_xq_y\sigma_y \\ & + \left(c_{11}q_x^2 + c_{22}q_y^2\right)\sigma_z + \left(d_{11}q_x^2 + d_{22}q_y^2\right)\sigma_0.\end{aligned} \tag{4}$$

By performing coordinate transformation, we may obtain the corresponding eigenvalues as

$$\begin{aligned}\mathcal{E}_{1,2} = {} & \alpha q^2 \pm \beta q^2 = d_{11}q_x^2 + d_{22}q_y^2 \\ & \pm \sqrt{\left(a_{12}{}^2 + b_{12}{}^2\right)q_x^2q_y{}^2 + \left(c_{11}q_x^2 + c_{22}q_y^2\right)^2},\end{aligned} \tag{5}$$

where α and β indicate two simplified expressions described as

$$\alpha = d_{11}\cos^2\theta + d_{22}\sin^2\theta,$$
$$\beta = \left\{\left(a_{12}^2 + b_{12}^2\right)\cos^2\theta\sin^2\theta + \left(c_{11}\cos^2\theta + c_{22}\sin^2\theta\right)^2\right\}^{\frac{1}{2}}, \quad (6)$$

with $q=\sqrt{q_x^2+q_y^2}$ and $\theta=\arctan\frac{q_y}{q_x}$. By examining the relation between two eigenvalues $\mathcal{E}_{1,2}=\alpha q^2 \pm \beta q^2$, we may obtain the fundamental features of quadratic nodal lines. For example, for a fixed angle θ, when $|\alpha| < \beta$, the first-order derivative of eigenvalues with respect to the wave vector q exhibits a typical type-I dispersion in the k_x-k_y plane, while when $|\alpha| > \beta$, the first-order derivative of eigenvalues exhibits a type-II dispersion. Particularly, when $|\alpha| = \beta$, the eigenvalues tend to display a type-III dispersion relation.

On the other side, considering that the inversion symmetry ($\mathcal{P}$), time-reversal symmetry ($\mathcal{T}$), and glide mirror symmetry ($\widetilde{M}_z$) exist in the k_z=0.0 plane of SG 129, nontrivial nodal lines should appear in this plane. Based on these symmetries, the effective Hamiltonian model for these nodal lines in the above particular plane can be written as

$$\mathcal{H}_{kp} = b_3 q_z \sigma_y + \left(c + c_1 q_x^2 + c_2 q_y^2 + c_3 q_z^2\right)\sigma_z + \left(a_1 q_x^2 + a_2 q_y^2 + a_3 q_z^2\right)\sigma_0. \quad (7)$$

Since the all degeneracy points in these nodal lines are characterized by q_z=0 and obey the relation $q=\sqrt{q_x^2+q_y^2}$, the corresponding eigenvalues are given by

$$\mathcal{E}_{1,2} = a_1 q^2\sin^2\theta + a_2 q^2\cos^2\theta \pm \left(c_1 q^2\sin^2\theta + c_2 q^2\cos^2\theta + c\right). \quad (8)$$

The above relation demonstrates that we may achieve a well-defined linear nodal ring, which is centered at the high-symmetry point Γ in reciprocal space.

In order to achieve the topological characteristics of various types of nodal lines and to explore further the existence of unusual nodal lines, we will systematically study all the nontrivial bands in the phonon spectra of some real material samples, i.e., a chiral crystal family BaXN$_2$ (X = Ti, Zr, Hf) in SG 129 ($P4/nmm$) [44,45] by using first-principles calculations. Particularly, we adopt the material sample BaZrN$_2$ as an example to perform our studies. Note that this material consists of 2 Ba, 2 Zr, and 4 N atoms in its first BZ, which are denoted by shiny red, dark green, and light purple balls in Fig. 2(a). The corresponding Wyckoff positions are 2c (0.5, 0.0, 0.1528) for Ba atoms, 2c (0.5, 0.0, 0.5871) for Zr atoms, 2b (0.5, 0.5, 0.5) and 2c (0.0, 0.5, 0.1755) for N atoms, and the bulk BZ, (001), and (110) surface BZs are also drawn in Fig. 2(b).

The band structure of the crystal BaZrN$_2$ is calculated by the density functional theory (DFT) using the Vienna *ab initio* Simulation Package (VASP) with the generalized gradient approximation (GGA) in the form of the Perdew-Burke-Ernzerhof (PBE) function for the exchange-correlation potential [48–50]. An accurate optimization of structural parameters is employed both by minimizing the interionic forces less than 0.001 eV/Å and a cutoff energy at 520 eV. The first

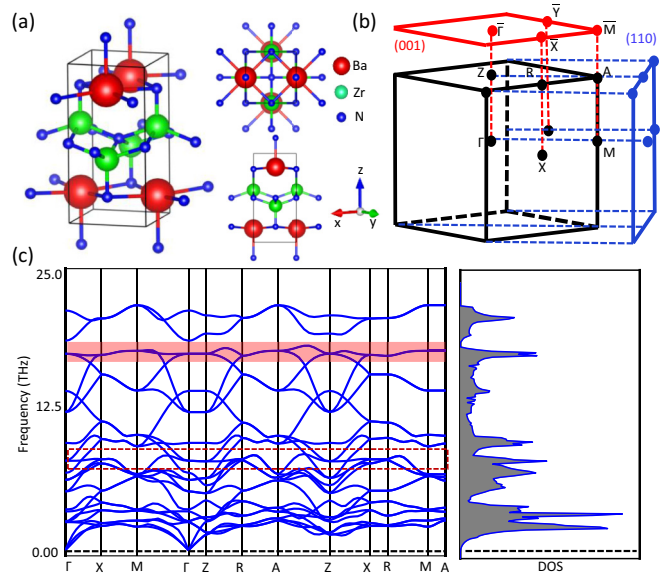

FIG. 2. (a) Crystalline structure the chiral crystal BaZrN$_2$ in a primitive cell, where the red (light green and dark blue) atoms stand for Ba (Zr and N) atoms. (b) Bulk BZ of BaZrN$_2$ and the corresponding (001) and (110) surface BZs. (c) Phononic spectrum of BaZrN$_2$ along high-symmetry paths and the corresponding local phononic DOS. The red box and red dotted line denote a chosen frequency regime ranging from 0 to 25.0 THz.

BZ is gridded with $6\times6\times6$ k points. Then the phononic spectrum is gained using the density-functional perturbation theory, implemented in thePHONOPY package [51,52]. The force constants are calculated by using a $2\times2\times1$ supercell. To reveal the topologically nontrivial nature of various phononic states in material samples, the phononic Hamiltonian is constructed by using the tight-binding model, and the surface local density of states (DOS) are calculated using the open-source software WANNIER TOOLS code [53] together with the surface Green's function [54]. Note that the crystal structures of all materials are constructed and obtained from the Materials Project [55].

III. RESULTS AND DISCUSSION

A. Butterfly-shape hourglass type-II nodal birdcage

Since every cell of the crystal BaXN$_2$ (X=Ti, Zr, Hf) is composed by 8 atoms, its phononic dispersion displays 24 phonon bands, including 3 acoustic and 21 optical branches. The disappearance of virtual frequency in phononic dispersion ensures the dynamical stability of material samples. In Fig. 2(c) we plot the phononic dispersion of BaZrN$_2$ along high-symmetry paths and the corresponding phononic DOS in the frequency regime ranging from 0 to 25 THz. Note that the phononic spectra of the other two material samples, i.e., BaHfN$_2$ and BaTiN$_2$ in this material family, are provided in the Supplemental Material (SM), Figs. S1 and S2 [56], respectively.

Through carefully examining the phononic dispersion of BaXN$_2$, we focus our investigations on three particular frequency regimes to reveal its unique topological features. First, we find that the degeneracy point contributed by the 14th and

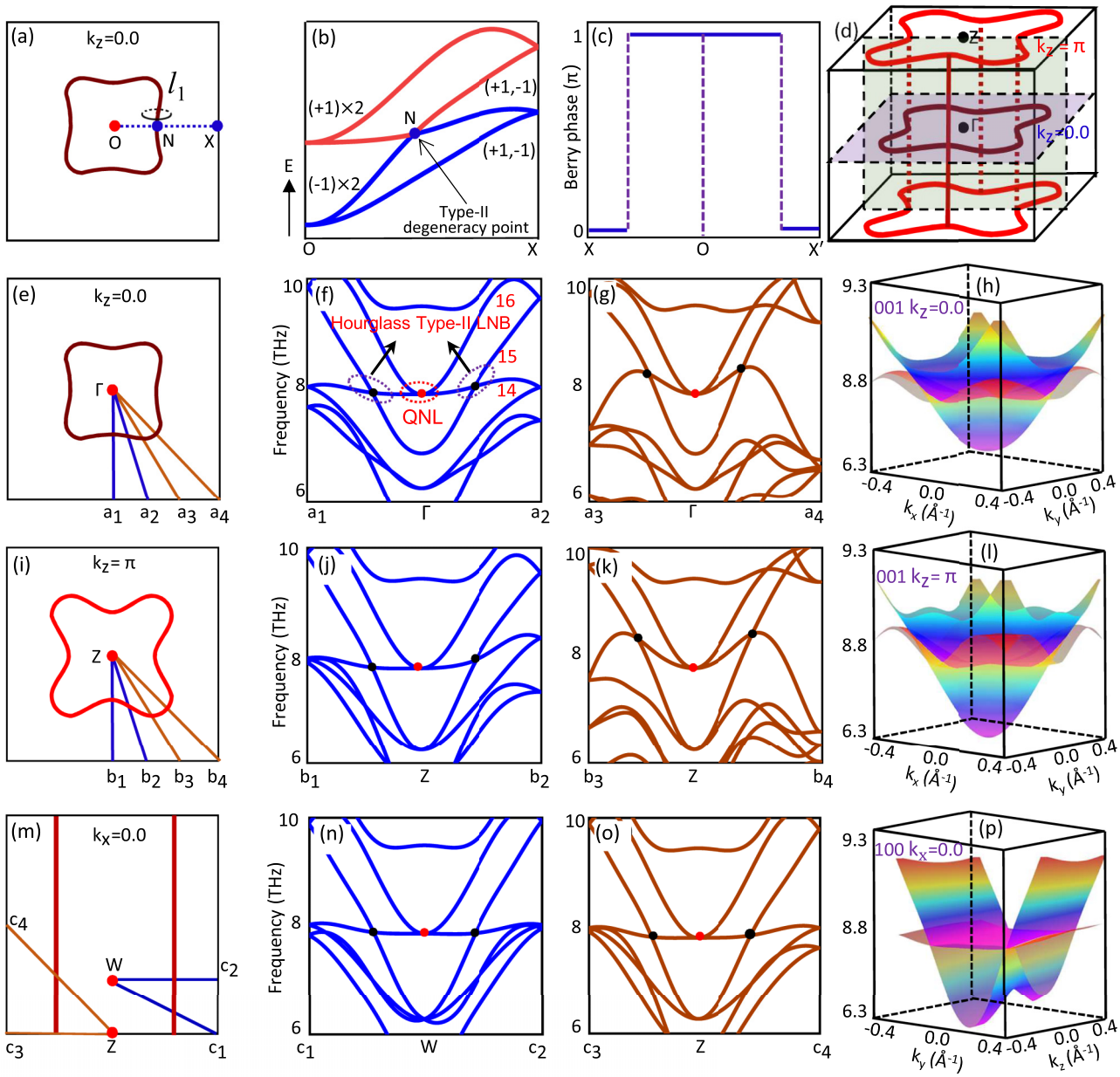

FIG. 3. (a) A nodal ring in a surface BZ and two time-reversal invariant momentum points O and X are chosen to form a linear path. (b) The bands with different irres to construct the degeneracy point N along the path O and X. (c) Spatial distribution of Berry phase when the closing path goes across the nodal line. (d) Spatial distribution of three node rings and four straight nodal lines between the 14th and 15th branches in the 3D BZ. (e) A butterfly-shape type-II nodal ring appears in the $k_z = 0.0$ plane and four typical paths Γ-a_n ($n = 1$–4) are chosen. (f), (g) Phononic dispersion along the paths a_1-Γ-a_2 and a_3-Z-a_4, respectively. (h) 3D phonon dispersion of butterfly-shape nodal ring in the $k_z = 0.0$ plane. (i) A butterfly-shape type-II nodal ring appears in the $k_z = \pi$ plane and four typical paths Z-b_n ($n = 1$–4) are chosen. (j), (k) Phonon dispersion along paths b_1-Z-b_2 and b_3-Z-b_4, respectively. (l) 3D phonon dispersion of the butterfly-shape nodal ring at the $k_z = \pi$ plane. (m) Spatial distribution of two type-II linear nodal lines appearing in the $k_x = 0.0$ plane and four typical paths $c_{1,2}$-W and $c_{3,4}$-Z are chosen. (n), (o) Phononic dispersion along paths c_1-W-c_2 and c_3-Z-c_4, respectively. (p) 3D phononic dispersion of type-II linear nodal in the $k_x = 0.0$ plane.

15th phonon branches, highlighted by the red dashed-line box, displays an obvious type-II dispersion along the paths Γ-X and Γ-M. By using symmetry analysis, we make sure that both planes localized at $k_z = 0$ and π are protected by the glide mirror symmetry $\widetilde{M}_z$, $\mathcal{P}$, and $\mathcal{T}$. Thus the degeneracy points in these two planes can be described by the effective Hamiltonian described in Eq. (7) and the corresponding eigenvalues are given by Eq. (8). Based on these messages, we may conclude that a nodal ring exists in every plane. To verify this conclusion and to obtain the topological features of nodal ring in the k_z=0 plane, we choose two time-reversal invariant momentum points O and X, which establish a straight line to cross this nodal ring at the point N as drawn in Fig. 3(a). Moreover, around this crossing point N, two associated band branches are drawn in Fig. 3(b). One may see that just crossing this point, both band branches change their irreducible representations (irres). By further calculating their first derivative of eigenvalues with respect to q and then examining its

derivative with respect to θ, we find that both branches form this degeneracy point and display a typical type-II dispersion, verifying that this nodal ring belongs to a linear type-II one.

To determine the nontrivial nature of this nodal ring, we may examine its Berry phase [57]. To the end, we choose a ringlike path l_1 to encircle the nodal ring near to the crossing point N as drawn in Fig. 3(a). Then the Berry phase along this path l_1 can be calculated by the following equation:

$$\gamma = \oint_C A(\mathbf{k}) \cdot d\mathbf{k}, \tag{9}$$

where $\mathbf{A}(\mathbf{k}) = -i \sum_m \langle u_m(\mathbf{k}) | \nabla_k | u_m(\mathbf{k}) \rangle$ is the Berry connection [58], $u_m(\mathbf{k})$ is the Bloch wave function of the mth phonon band, and C is a closed path in momentum space (i.e., l_1 adopted here). In a similar way, the nontrivial topology of the calculated Berry phases for the remaining nodal rings or lines can be confirmed. The calculated result of Berry phase for path l_1 is given in Fig. 3(c) and clearly demonstrates that along this closed path, the related Berry phase equals a nonzero value π, confirming well its nontrivial nature.

To glimpse the whole geometrical configuration of the nodal ring appearing in the plane with $k_z = 0$, we focus our attention on the phononic dispersion in the one-eighth regime of surface BZ, as drawn in Fig. 3(e), in which some typical paths Γ-a_n ($n = 1$–4) are chosen. The phononic bands along the paths a_1-Γ-a_2 and a_3-Γ-a_4 are plotted in Figs. 3(f) and 3(g), respectively. One may see that along the path a_1-Γ, the crossing point between the 14th and 15th bands possesses a typical type-II linear dispersion relation and meanwhile, along the path Γ-a_2, the crossing point between these two bands displays a similar dispersion relation with completely opposite slopes. Considering the spatial distributions of the 13th–16th bands, these two degeneracy points can be also classified further into type-II hourglass nodal points. Moreover, along the paths a_3-Γ and Γ-a_4, two similar type-II nodal points appear between the 14th and 15th bands [see Fig. 3(g)]. Considering the spatial distributions of the above four nodal points, together with the screw rotation symmetry $\widetilde{C}_{4z}$ and the glide mirror symmetry $\widetilde{M}_z$ in this plane, we may conclude the geometrical configuration of the nodal ring in the $k_z = 0$ plane displays a butterfly-shape type-II linear nodal ring as drawn in Fig. 3(e), which is also confirmed well by its 3D map perspective versus the frequency in the k_x-k_y plane as plotted in Fig. 3(h). In a similar way, we also uncover that the nodal ring in the $k_z = \pi$ plane also displays as a butterfly-shape type-II linear nodal ring, as illustrated in Figs. 3(i)–3(l).

Furthermore, to obtain the overall morphology of nodal-line phonons in this real material, we tend to study the phononic dispersion in the plane with $k_x = 0.0$, which is perpendicular to the above two planes. Considering that the mirror symmetry $\mathcal{M}_x$, the screw rotation symmetry $\widetilde{C}_{2y}$, and $\mathcal{T}$ exist in this plane, two nodal lines, which are contributed by the 14th and 15th band branches, should be generated. To verify this conclusion, we plotted these two nodal lines according to the associated degeneracy points in the phononic spectrum in Fig. 3(m). Note that a particular point W with the coordinates (0.0, 0.0, 0.24), which denotes a triple degenerate point contributed by the 12th, 13th, and 14th bands, is also given in this plane. To achieve the topological categories and the detailed geometric configurations of these nodal lines, we have chosen four typical paths $c_{1(2)}$-W and $c_{3(4)}$-Z, and the corresponding phononic bands are drawn in Figs. 3(n) and 3(o), respectively. One may see that along these paths, four type-II nodal points still exist, indicating that two corresponding nodal lines belong to the type-II one. Moreover, the related 3D map of these nodal points in the k_y-k_z plane are also plotted in Fig. 3(p). It clearly demonstrates that these two nodal lines are nearly completely straight, as drawn in Fig. 3(m). Considering further the screw rotation symmetry ($\widetilde{C}_{4z}$) in this material, another pair of type-II straight nodal lines exist in its perpendicular plane with $k_y = 0$, as drawn in Fig. 3(d). More interestingly, these two pairs of straight nodal lines just connect with the previous three nodal rings in the planes $k_z = 0$ and $\pm\pi$ to form a butterfly-shape hourglass type-II nodal birdcage as drawn in Fig. 3(d), which has rarely been reported previously in real materials.

B. Nontrivial surface states induced by the type-II nodal birdcage

In what follows we study the nontrivial surface states induced by the butterfly-shape type-II nodal-birdcage phonons in the material $BaZrN_2$. Firstly, we plot a part of its phononic dispersion and the corresponding projection of phonon DOS in the frequency regime ranging from 6 to 10 THz in the (001) surface BZ along the high-symmetry paths $\overline{Y}$-$\overline{\Gamma}$-$\overline{X}$-$\overline{M}$-$\overline{\Gamma}$-$\bar{a}_3$ in Fig. 4(a). It clearly demonstrates that around the projection point $\overline{\Gamma}$ and in the frequency regime from 8.0 to 8.5 THz, several projected crossing points displaying an hourglasslike type-II dispersion relation appear, confirming well the existence of type-II hourglass nodal rings discussed previously.

Not only that, we also find several surface arc states induced by the type-II linear nodal birdcage as drawn in Fig. 4(a). Between two neighboring crossing points formed by type-II surface-state branches there exist distinct nontrivial drumheadlike surface states that are produced by the butterfly-shape type-II nodal birdcage. To demonstrate this finding, we focus our investigations on three particular surface-state regimes as denoted by dashed-line loops ①, ②, and ③ in Fig. 4(a) and enlarge them in Figs. 4(b)–4(d), respectively, where the projection points $\bar{d}_{1,3,4}$ and $\bar{e}_{1,3,4}$ from $d_{1,3,4}$ and $e_{1,3,4}$ are also highlighted. Note that the three points $d_{1,3,4}$ and the other three points $e_{1,3,4}$ are chosen from the butterfly-shape nodal ring located in the $k_z = 0$ plane and the similar nodal ring in the $k_z = \pi$ plane (see Fig. 3). We may find that there exists a nontrivial surface arc connecting with two neighboring projection points $\bar{d}_1$ and $\bar{e}_1$ ($\bar{d}_3$ and $\bar{e}_3$, $\bar{d}_4$ and $\bar{e}_4$), confirming further the topologically nontrivial nature of the butterfly-shape type-II nodal birdcage observed in this material. To further examine their nontrivial features, the associated isofrequency surface projections at the frequency regime ranging from 7.93 to 8.45 THz on the (001) surface BZ are also calculated as drawn in Figs. 4(e) and 4(f), respectively. We may see that the contour plot of the phononic local DOS associated with the spatial distribution of isofrequency surface states agrees well with the drumheadlike surface states. Moreover, due to the fourfold rotation symmetry (C_{4z}) in this material, the phononic surface states exhibit a distinct square-shaped geometric symmetry within the surface BZ. To present comparable studies between the butterfly-shaped hourglass

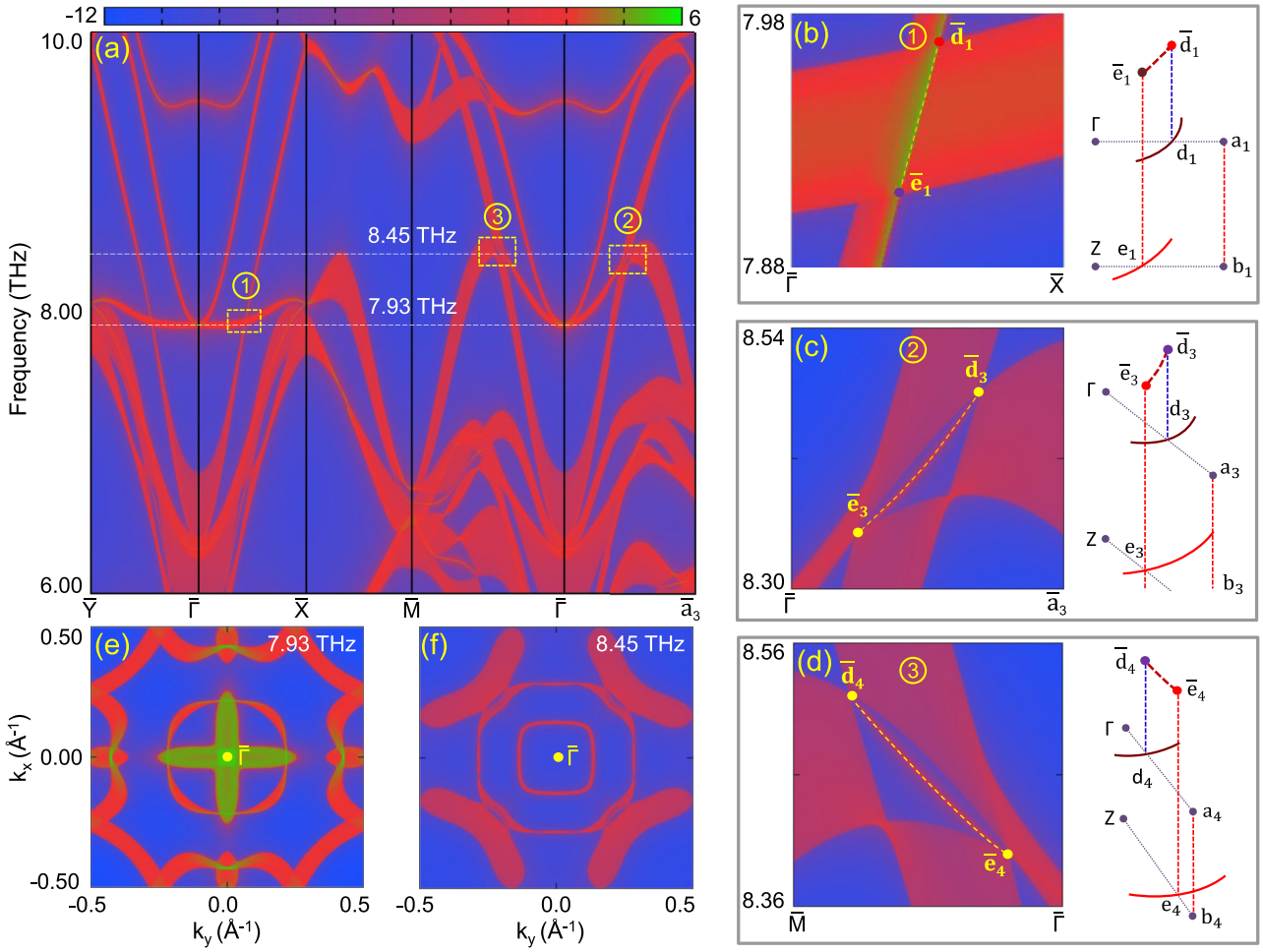

FIG. 4. (a) Surface states of $BaZrN_2$ in the (001) surface BZ along the high-symmetry paths $\overline{X}$-$\overline{\Gamma}$-$\overline{Y}$-$\overline{M}$-$\overline{\Gamma}$-$\bar{a}_3$ in the frequency regime ranging from 6 to 10 THz. (b)–(c) Three drumheadlike surface states induced by the type-II nodal birdcage, which are highlighted by three dashed-line boxes in the figure (a). (e) and (f) Isofrequency surface contours at 7.9 and 8.4 THz in the (001) surface BZ to demonstrate the existence of butterfly-shape type-II nodal birdcage and anisotropic quadratic nodal line.

nodal-birdcage phonon and the linear nodal-line phonon, we provide more details to show the nontrivial phononic states and the unique nontrivial properties in other family materials $BaXN_2$ (X = Ti, Zr, and Hf) in the SM, Sec. B [56].

C. Three kinds of unusual nodal-line phonons

Let's take a look back at the phononic dispersion drawn in Figs. 3(f), 3(j), and 3(n). We may find that the 15th and 16th phononic branches in the material $BaZrN_2$ display a distinctive quadratic nodal line along the high-symmetry path Γ-Z, which is protected both by the screw rotation symmetry $\widetilde{C}_{4z}$ and the mirror symmetry $\mathcal{M}_x$. Through examining the dispersion relation of the typical degeneracy points at points Γ, W, and Z in this quadratic nodal line, we find the band branches along the k_x and k_y directions exhibit a typical type-III feature, while along other directions, such as the 110 direction in the $k_x = k_y$ plane, they display type-II features, indicating that along different directions of the same degeneracy point in a nodal line the related dispersion relations belong to completely different categories. We refer to this quadratic nodal line as an anisotropic one. To demonstrate further this anisotropic behavior, we present the corresponding 3D phononic dispersion covering points Γ and Z in the k_x-k_y plane in the SM, Figs. S3(e) and S3(f) [56], and that of the k_x-k_z plane and the (110) plane in SM Figs. S4(a)–S4(d) [56]. These 3D maps confirm further the anisotropic characteristic of this quadratic nodal line by exhibiting type-II and -III dispersion relations in its different momentum directions.

It is interesting that the quadratic nodal line along the high-symmetry path Γ-Z in another frequency regime displays completely different dispersion relations in the materials $BaXN_2$ (X = Zr and Hf). To highlight this finding, we plot the 21st and 22nd band branches around three typical points with different frequency values, i.e., point Γ along different directions, the point with $k_z = 0.08$, and point Z in Fig. 5(a). At these three points there are just three band crossings contributing to form the above quadratic nodal line. One may see that at Γ, the degeneracy point displays a type-II dispersion relation in all momentum directions [see upper panel in Figs. 5(a) and 5(b)]. Nevertheless, around the point $k_z = 0.08$ with $k_x = k_y = 0.0$, the phononic dispersion of the degeneracy point shows another type of dispersion relation different from

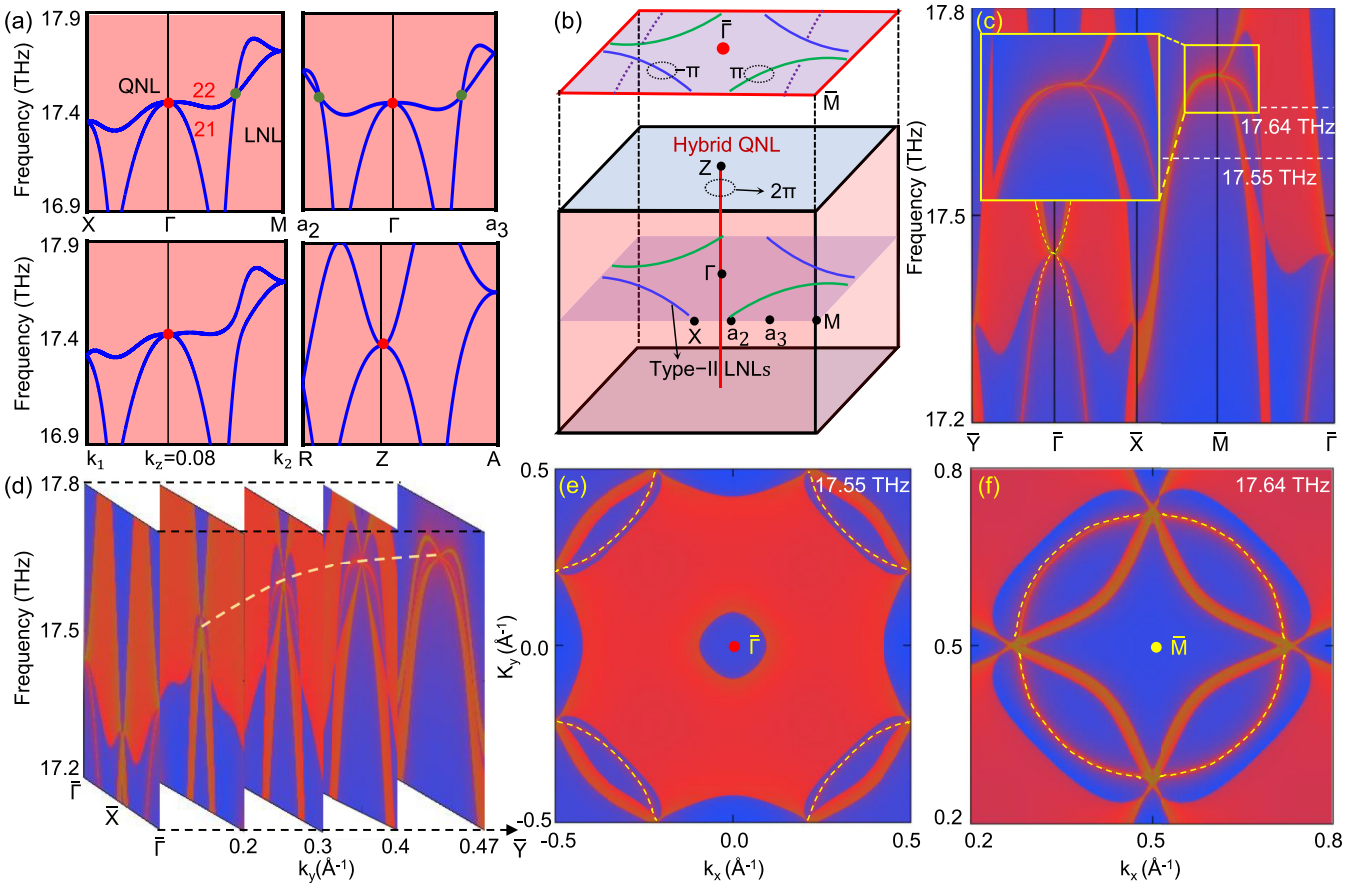

FIG. 5. (a) Phononic spectra on three typical planes with $k_z = 0$, $k_z = 0.08$ and $k_z = \pi$, in which the related high-symmetry paths are chosen as X-Γ-M, a_2-Γ-a_3, k_1-($k_z = 0.08$)-k_2 with $k_1 = (0.5, 0.0, 0.08)$ and $k_2 = (0.5, 0.5, 0.08)$ and R-Z-A. (b) Spatial distributions of node lines between the 21th and 22th band branches, where the green (blue) type-II linear nodal lines have positive (negative) Berry phase on the $k_z = 0.0$ plane. Here, a hybrid quadratic nodal line (HQL, colored by red) along the path Γ-Z. (c) Phononic surface states of $BaZrN_2$ in the (001) surface BZ along the $\overline{Y}$-$\overline{\Gamma}$-$\overline{X}$-$\overline{M}$-$\overline{\Gamma}$ in the frequency regime ranging from 17.2 to 17.8 THz. (d) Evolution of the nontrivial phononic surface states with the increasing frequency k_y along the $\overline{\Gamma}$-$\overline{X}$-$\overline{\Gamma}$ direction. (e) and (f) Two typical isofrequency surfaces contour at the frequency 17.55 and 17.68 THz on the (001) surface BZ.

the previous one, i.e., a type-II dispersion along the k_x direction, while there is a type-I dispersion along the 110 direction, especially along path Z-($k_z = 0.2$). Particularly, around point Z, the phononic dispersion of degeneracy point is evolved into a perfect type-I feature [see the fourth panel in Fig. 5(a)]. Obviously, in the different sections of this nodal line, the phononic dispersion relations belong to different categories. To differentiate this nodal line from others, we refer to it as a hybrid quadratic nodal line. It is stressed that the projected surface states in the phononic spectrum around projection point $\overline{\Gamma}$ [see Fig. 5(c), highlighted by yellow dash lines] and the corresponding 3D map (see SM Figs. S4(e)–S4(h) [56]) confirm well its hybrid dispersion relation.

Apart from two unusual quadratic nodal-line phonons, it is inspiring that another unconventional linear nodal-line phonon appears also in these material samples. By examining the 21st and 22nd phononic bands along paths Γ-M, Γ-a_2, and Γ-a_3 drawn in Fig. 5(a), we find that there exist some degeneracy points displaying a type-II dispersion relation. It is stressed that due to the glide mirror symmetry $\widetilde{M}_z$, $\mathcal{P}$, and $\mathcal{T}$ existed in the $k_z = 0.0$ plane; the degeneracy points in this plane tend to form four linear nodal lines. Moreover, our further calculations demonstrate that two of them have a positive Berry phase π and the other two have a negative one $-\pi$, which are highlighted by different colors as drawn in Fig. 5(b), verifying well their nontrivial features. Interestingly, these linear nodal lines are characterized by another unusual feature that every nodal line is adjacent to but not in contact with the boundaries of BZ. To verify their nontrivial features, we plot the projections of phononic local DOS in the frequency regime ranging from 17.2 to 17.8 THz on the (001) surface BZ along the high-symmetry paths $\overline{Y}$-$\overline{\Gamma}$-$\overline{X}$-$\overline{M}$-$\overline{\Gamma}$ in Fig. 5(c). One may find that along the projection path $\overline{X}$-$\overline{M}$, a visible drumheadlike surface state displays well, and it should be induced by a pair of nodal lines with opposite Berry phases [see an enlarged inset panel in Fig. 5(c)]. It is noted that both the appearance of a drumheadlike surface state and its evolution process versus the momentum k_y [see Fig. 5(d)] further confirm the nontrivial features of this pair of linear nodal lines. Furthermore, two typical isofrequency surfaces which are centered at point $\overline{\Gamma}$ [see Fig. 5(e)] and point $\overline{M}$ [see Fig. 5(f)] also clearly display the projections of two pairs of linear nodal lines, verifying well their spatial distribution and geometric configurations described in Fig. 5(b).

IV. CONCLUSIONS

In summary, we have presented the basic categories of topological nodal lines according to the dispersion relations of degeneracy points in them, and based on these basic categories, we have proposed some unusual topological nodal lines existing in real materials. By performing symmetry analysis in combination with the first-principles calculations, we have uncovered a series of novel topological nodal-line phonons in a material family, i.e., BaXN$_2$ (X = Ti, Zr, and Hf) in SG 129, which includes a butterfly-shape hourglass type-II nodal-birdcage phonon and three kinds of unusual nodal-line phonons. The nodal-birdcage phonons are composed of three butterfly-shape nodal rings and four straightly linear nodal lines in their phonon spectra. It is interesting that some nodal lines in this nodal birdcage display unconventional hourglasslike features. More importantly, three kinds of unusual nodal-line phonons, including the anisotropic, hybrid quadratic nodal line and two pairs of linear nodal lines adjacent to the boundaries of BZ, also appear in this material family. The topologically nontrivial features of these various nodal lines are confirmed by their Berry-phase calculations and the drumheadlike surface states in the related surface BZs. Our theoretical results provide an ideal material platform to study various novel topological nodal-line phonons, including butterfly-shape hourglass type-II nodal-birdcage phonons and three unusual nodal-line phonons.

ACKNOWLEDGMENTS

This work is supported by the National Science Foundation of China with Grants No. 11774104, No. U20A2077, and No. 12147113, and partially by the National Key R&D Program of China (2021YFC2202301).

[1] C. Fang, M. J. Gilbert, X. Dai, and B. A. Bernevig, Multi-Weyl topological semimetals stabilized by point group symmetry, Phys. Rev. Lett. **108**, 266802 (2012).

[2] F. de Juan, A. G. Grushin, T. Morimoto, and J. E. More, Quantized circular photogalvanic effect in Weyl semimetals, Nat. Commun. **8**, 15995 (2017).

[3] H. Miao, T.-T. Zhang, L. Wang, D. Meyers, A.-H. Said, Y.-L. Wang, Y.-G. Shi, H.-M. Weng, Z. Fang, and M.-P.-M. Dean, Observation of double Weyl phonons in parity-breaking FeSi, Phys. Rev. Lett. **121**, 035302 (2018).

[4] Z. K. Liu, B. Zhou, Y. Zhang, Z. J. Wang, H. M. Weng, D. Prabhakaran, S.-K. Mo, Z. X. Shen, Z. Fang, X. Dai, and Y. L. Chen, Discovery of a three-dimensional topological Dirac semimetal, Na_3Bi, Science **343**, 864 (2014).

[5] X. Huang, L. Zhang, Y. Long, P. Wang, D. Chen, Z. Yang, H. Liang, M. Xue, H. Weng, Z. Fang, X. Dai, and G. Chen, Obversation of the chiral-anomaly-induced negative magnetoresistance in 3D Weyl semimetal TaAs, Phys. Rev. X **5**, 031023 (2015).

[6] C. Fang, L. Lu, J. Liu, and L. Fu, Topological semimetals with helicoid surface states, Nat. Phys. **12**, 936 (2016).

[7] R. M. Geilhufe, S. S. Borysov, A. Bouhon, and A. V. Balatsky, Data mining for three-dimensional organic Dirac materials: Focus on space group 19, Sci. Rep. **7**, 7298 (2017).

[8] T.-T. Zhang, Z. D. Song, A. Alexandradinata, H.-M. Weng, C. Fang, L. Lu, and Z. Fang, Double-weyl phonons in transition-metal monosilicides, Phys. Rev. Lett. **120**, 016401 (2018).

[9] M. Bruni, C. Germani, and R. Maartensa, Gravitational collapse on the Brane: A no-go theorem, Phys. Rev. Lett. **87**, 231302 (2001).

[10] W.-C. Ji and J.-R. Shi, Topological phonon modes in a two-dimensional Wigner crystal, Chin. Phys. Lett. **34**, 036301 (2017).

[11] V. Peri, M. Serra-Garcia, R. Ilan, and S. D. Huber, Axial-field induced chiral channels in an acoustic Weyl system, Nat. Phys. **15**, 357 (2019).

[12] B. Bradlyn, J. Cano, Z. Wang, M. G. Vergniory, C. Felser, R. J. Cava, and B. A. Bernevig, Beyond Dirac and Weyl fermions: Unconvertianl quasiparticles in conventional crystals, Science **353**, aaf5037 (2016).

[13] Q.-B. Liu, Y. Qian, H.-H. Fu, and Z. Wang, Symmetry-enforced Weyl phonons, npj Comput. Mater. **6**, 95 (2020).

[14] J. X. Li, Q. Xie, S. Ullah, R. H. Li, H. Ma, D. Z. Li, Y. Y. Li, and X. Q. Chen, Coexistent three-component and two-component Weyl phonons in TiS, ZrSe, and HfTe, Phys. Rev. B **97**, 054305 (2018).

[15] Q.-B. Liu, Z. Wang, and H.-H. Fu, Charge-four Weyl phonons, Phys. Rev. B **103**, L161303 (2021).

[16] B. W. Xia, R. Wang, Z. J. Chen, Y. J. Zhao, and H. Xu, Symmetry-protected ideal type-II Weyl phonons in CdTe, Phys. Rev. Lett. **123**, 065501 (2019).

[17] S. Vaidya, J. Noh, A. Cerjan, C. Jörg, G. von Freymann, and M. C. Rechtsman, Observation of a charge-2 photonic Weyl point in the infrared, Phys. Rev. Lett. **125**, 253902 (2020).

[18] R. Wang, B. W. Xia, Z. J. Chen, B. B. Zheng, Y. J. Zhao, and H. Xu, Symmetry-protected topological triangular Weyl complex, Phys. Rev. Lett. **124**, 105303 (2020).

[19] L. Lu, Z.-Y. Wang, D.-X. Ye, L.-X. Ran, L. Fu, J. D. Joannopoulos, and M. Soljačić, Experimental observation of Weyl points, Science **349**, 622 (2015).

[20] Q.-B. Liu, H.-H. Fu, and R. Wu, Topological phononic nodal hexahedron net and nodal links in the high-pressure phase of the semiconductor CuCl, Phys. Rev. B **104**, 045409 (2021).

[21] B. Zheng, B. Xia, R. Wang, Z. Chen, J. Zhao, Y. Zhao, and H. Xu, Ideal type-III nodal-ring phonons, Phys. Rev. B **101**, 100303(R) (2020).

[22] J.-Y. You, X.-L. Sheng, and G. Su, Topological gimbal phonons in T-carbon, Phys. Rev. B **103**, 165143 (2021).

[23] X. Zhang, Z.-M. Yu, Y. Lu, X.-L. Sheng, H. Y. Yang, and S. A. Yang, Hybrid nodal loop metal: Unconventional magnetoresponse and material realization, Phys. Rev. B **97**, 125143 (2018).

[24] B. B. Zheng, F. Y. Zhan, X. Z. Wu, R. Wang, and J. Fan, Hourglass phonons jointly protected by symmorphic and nonsymmorphic symmetries, Phys. Rev. B **104**, L060301 (2021).

[25] Q.-F. Liang, J. Zhou, R. Yu, Z. Wang, and H. Weng, Node-surface and node-line fermions from nonsymmorphic lattice symmetries, Phys. Rev. B **93**, 085427 (2016).
[26] W. Wu, Y. Liu, S. Li, C. Zhong, Z.-M. Yu, X.-L. Sheng, Y. X. Zhao, and S. A. Yang, Nodal surface semimetals: Theory and material realization, Phys. Rev. B **97**, 115125 (2018).
[27] O. Türker and S. Moroz, Weyl nodal surfaces, Phys. Rev. B **97**, 075120 (2018).
[28] Q.-B. Liu, Z.-Q. Wang, and H.-H. Fu, Ideal topological nodal-surface phonons in RbTeAu-family materials, Phys. Rev. B **104**, L041405 (2021).
[29] C. Xie, H. Yuan, Y. Liu, X. Wang, and G. Zhang, Three-nodal surface phonons in solid-state materials: Theory and material realization, Phys. Rev. B **104**, 134303 (2021).
[30] Q.-B. Liu, H.-H. Fu, G. Xu, R. Yu, and R. Wu, Categories of phononic topological Weyl open nodal lines and a potential material candidate: $Rb_2Sn_2O_3$, J. Phys. Chem. Lett. **10**, 4045 (2019).
[31] H. Weng, Y. Liang, Q. Xu, R. Yu, Z. Fang, X. Dai, and Y. Kawazoe, Topological node-line semimetal in three-dimensional graphene networks, Phys. Rev. B **92**, 045108 (2015).
[32] R. Yu, H. Weng, Z. Fang, X. Dai, and X. Hu, Topological node-line semimetal and Dirac semimetal state in antiperovskite Cu_3PdN, Phys. Rev. Lett. **115**, 036807 (2015).
[33] S. Li, Y. Liu, S.-S. Wang, Z.-M. Yu, S. Guan, X.-L. Sheng, Y. Yao, and S. A. Yang, Nonsymmorphic-symmetry-protected hourglass Dirac loop, nodal line, and Dirac point in bulk and monolayer X_3SiTe_6 (X = Ta, Nb), Phys. Rev. B **97**, 045131 (2018).
[34] J. Li, Q. Xie, J. Liu, R. Li, M. Liu, L. Wang, D. Li, Y. Li, and X.-Q. Chen, Phononic Weyl nodal straight lines in MgB_2, Phys. Rev. B **101**, 024301 (2020).
[35] S. Li, Z.-M. Yu, Y. Liu, S. Guan, S.-S. Wang, X. Zhang, Y. Yao, and S. A. Yang, Type-II nodal loops: Theory and material realization, Phys. Rev. B **96**, 081106(R) (2017).
[36] X.-M. Zhang, L. Jin, X.-F. Dai, and G.-D. Liu, Topological type-II nodal line semimetal and Dirac semimetal state in stable kagome compound Mg_3Bi_2, J. Phys. Chem. Lett. **8**, 4814 (2017).
[37] Z.-M. Yu, W. Wu, X.-L. Sheng, Y. X. Zhao, and S. A. Yang, Quadratic and cubic nodal lines stabilized by crystalline symmetry, Phys. Rev. B **99**, 121106(R) (2019).
[38] G. Liu, Y. Jin, Z. Chen, and H. Xu, Symmetry-enforced straight nodal-line phonons, Phys. Rev. B **104**, 024304 (2021).
[39] C. Chen, S.-S. Wang, L. Liu, Z.-M. Yu, X.-L. Sheng, Z. Chen, and S. A. Yang, Ternary wurtzite CaAgBi materials family: A playground for essential and accidental, type-I and type-II Dirac fermions, Phys. Rev. Mater. **1**, 044201 (2017).
[40] X. Wang, T. Yang, Z. Cheng, G. Surucu, J. Wang, F. Zhou, Z. Zhang, and G. Zhang, Topological nodal line phonons: Recent advances in materials realization, Appl. Phys. Rev. **9**, 041304 (2022).
[41] Z.-M. Yu, Z. Zhang, G.-B. Liu, W. Wu, X.-P. Li, R.-W. Zhang, S. A. Yang, and Y. Yao, Encyclopedia of emergent particles in three-dimensional crystals, Sci. Bull. **67**, 375 (2022).
[42] G. Ding, T. Sun, and X. Wang, Ideal nodal-net, nodal-chain, and nodal-cage phonons in some realistic materials, Phys. Chem. Chem. Phys. **24**, 11175 (2022).
[43] F. Zhou, Z. Yang, H. Chen, M. Kuang, T. Yang, and X. Wang, Hybrid-type nodal ring phonons and coexistence of higher-order quadratic nodal line phonons in an AgZr alloy, Phys. Rev. B **104**, 174108 (2021).
[44] O. Seeger, M. Hofmann, J. Strähle, J. P. Laval, and B. Frit, Synthesis and structure of $Ba[ZrN_2]$ and $Ba_2[NbN_3]$, Z. Anorg. Allg. Chem. **620**, 2008 (1994).
[45] D. H. Gregory, M. G. Barker, P. P. Edwards, M. Slaski, and D. J. Siddons, Synthesis, structure, and magnetic properties of the new ternary nitride $BaHfN_2$ and of the $BaHf_{1-x}Zr_xN_2$ solid solution, J. Solid State Chem. **137**, 62 (1998).
[46] M. Wang, Y. Wang, Z. Yang, J. Fan, B. Zheng, R. Wang, and X. Wu, Symmetry-enforced nodal cage phonons in Th_2BC_2, Phys. Rev. B **105**, 174309 (2022).
[47] T. Yang, Y. Gao, L. Hao, H. Zhang, X. Tan, P. Wang, Z. Cheng, and W. Wu, Cladded phononic nodal frame state in biatomic alkali-metal sulfides, Phys. Rev. B **108**, 134310 (2023).
[48] W. Kohn and L. J. Sham, Self-consistent equations including exchange and correlation effects, Phys. Rev. **140**, A1133 (1965).
[49] P. E. Blöchl, Projector augmented-wave method, Phys. Rev. B **50**, 17953 (1994).
[50] J. P. Perdew, K. Burke, and M. Ernzerhof, Generalized gradient approximation made simple, Phys. Rev. Lett. **77**, 3865 (1996).
[51] A. Carreras, A. Togo, and I. Tanaka, DynaPhoPy: A code for extracting phonon quasiparticles from molecular dynamics simulations, Comput. Phys. Commun. **221**, 221 (2017).
[52] A. Togo and I. Tanaka, First principles phonon calculations in materials science, Scr. Mater. **108**, 1 (2015).
[53] Q.-S. Wu, S.-N. Zhang, H.-F. Song, M. Troyer, and A. A. Soluyanov, WannierTools: An open-source software package for novel topological materials, Comput. Phys. Commun. **243**, 81 (2019).
[54] M. P. L. Sancho, J. M. L. Sancho, J. M. L. Sancho, and J. Rubio, Highly convergent schemes for the calculations of bulk and surface Green functions, J. Phys. F: Met. Phys. **15**, 851 (1985).
[55] H. Geoffroy, F. Chris, E. Virginie, J. Anubhav, and C. Gerbrand, Data mined ionic substitutions for the discovery of new compounds, Inorg. Chem. **50**, 656 (2011).
[56] See Supplemental Material at http://link.aps.org/supplemental/10.1103/PhysRevB.109.155414 in which we provide more details regarding the phononic spectra, crystal structures, various nontrivial nodal-line phonons, and the 3D phononic dispersion of some unusual nodal-line phonons in some other family materials.
[57] Y. Suzumura and A. Yamakage, Berry phase of Dirac nodal line semimetal in single-component molecular conductor, J. Phys. Soc. Jpn. **87**, 093704 (2018).
[58] T. Qin, J. Zhou, and J. Shi, Berry curvature and the phonon Hall effect, Phys. Rev. B **86**, 104305 (2012).